Spatial extension of the mid to late Holocene sedimentary record of tsunamis along the Southern Kuril Trench, Hokkaido Japan

Ryo Nakanishi[1,2], Juichiro Ashi[1,2], Yosuke Miyairi[1], and Yusuke Yokoyama[1,3,4,5,6]

[1]Atmosphere and Ocean Research Institute, The University of Tokyo, Kashiwa, 277-8564, Japan.

[2]Graduate School of Frontier Sciences, University of Tokyo, Kashiwa, 277-8561, Japan.

[3]Department of Earth and Planetary Sciences, Graduate School of Science, The University of Tokyo, Japan.

[4]Graduate Program on Environmental Science, Graduate School of Arts and Sciences, The University of Tokyo, Japan.

[5]Japan Agency for Marine-Earth Science and Technology (JAMSTEC), Japan.

[6]Research School of Physics, The Australian National University, Canberra, ACT0200, Australia.

Corresponding author: Ryo Nakanishi (n-ryo@g.ecc.u-tokyo.ac.jp)

Key Points:

- Geological surveys performed along southeastern Hokkaido, Japan, document tsunamis originating from the Kuril Trench over 4000 years
- The 17th-century sand layer in Erimo was simulated as a tsunami following a Mw~8.8 earthquake model
- ^{14}C dating shows good agreement with tsunami ages in the surrounding regions, suggesting that Kuril tsunamis have reached more western areas

Abstract

Infrequent megathrust earthquakes, with their complex cycles and rupture modes, require a high-resolution spatiotemporal record of tsunami inundation over thousands of years for more accurate long-term predictions. Geological records suggest that prior to the 17th century, Mw>8 earthquakes on the Kuril Trench occurred at intervals of several hundred years. However, uncertainties remain about the rupture zone, owing to limited survey areas and chronological data. Therefore, we investigated tsunami deposits in a coastal wetland of southeastern Hokkaido, Japan, to characterize tsunamis originating from the Kuril Trench over the last 4000 years. On the eastern Erimo coast, ten sand layers were identified that exhibit the common features of tsunami deposits, such as a sheet distribution of several hundred meters, normal grading structure, and a sharp basal contact. According to numerical simulations, the 17th-century sand layer could be reproduced by tsunamis generated using a multiple rupture zone model (Mw~8.8). We used high-resolution radiocarbon dating and tephras to correlate tsunami deposits from the last 4000 years with those reported from regions ~100 km away. The tsunami history revealed by this study show good agreement with those of the compared regions. However, paleo-tsunamis reported from regions > 200 km away include some events that differ from those in this study, suggesting a diversity of Mw>8 earthquakes in the Kuril Trench. We clarified the history and extent of earthquake-generated tsunamis along the southwestern end of the Kuril Trench, which was previously unknown. Our results provide a framework for magnitude estimations and long-term prediction of earthquakes.

Plain Language Summary

Geological evidence over the past several thousand years is essential to improve the long-term predictions of giant earthquakes with recurrence intervals of several hundred years. The correlation of tsunamigenic traces along the Kuril Trench, especially on the southwestern coast, are unclear, hence, it is difficult to obtain information about the recurrence intervals and rupture zone of low-frequency earthquakes. Therefore, we investigated sedimentary records of tsunamis in the southwestern end coast along the Kuril Trench. We newly found the ten layers of sandy tsunami deposits and determined their ages. The tsunami ages over the past 4000 years are consistent with the tsunami history reported in the surrounding areas, indicating the large tsunami spreading along a wider coastline than previously known. The possible presence of such tsunamis is also supported by the numerical modeling of the tsunami caused by the Mw~8.8 earthquake in the 17th century. The tsunami history revealed in this area will provide a framework for future paleo-tsunami studies in the southern Kuril Trench.

Keywords: Tsunami deposits, Kuril Trench, Radiocarbon dating, Numerical simulation, Hokkaido

1 Introduction

Low-frequency megathrust earthquakes (e.g., the 1700 Cascadia, 1960 Chile, 2004 Sumatra, and 2011 Tohoku-oki earthquakes) have been reported to occur over wider rupture zones and prolonged occurrence intervals for hundreds to thousands of years, than the M7–8 earthquakes (Sieh et al., 2008; Goldfinger et al., 2013; Philibosian & Meltzner, 2020; Salditch et al., 2020). To study these low-frequency megathrust earthquakes, prehistorical data with timescales ranging from thousands to tens of thousands of years are required. Prehistoric data may be obtained solely from geologic records. For instance, these data can be obtained from uplifted terraces, deep-sea turbidites, and tsunami deposits (Goldfinger et al., 2013; Satake, 2015; Hutchinson & Clague, 2017). Every subduction zone has a high risk of M~9 earthquakes recurrence because the instrumentally recorded earthquakes do not relieve strain completely. Therefore, it is necessary to investigate case studies of low-frequency megathrust earthquakes from various regions as event clusters and the changes in the rupture zone patterns differs for each subduction zone (Nelson et al., 2006; Philibosian & Meltzner, 2020; Salditch et al., 2020).

Based on the instrumental observations obtained from the past 200 years in the southern part of the Kuril Trench, Mw7–8 earthquakes are known to occur with intervals of 50–100 years, with the Tokachi-oki or Nemuro-oki segments acting as rupture faults (Satake, 2015; Sawai, 2020). In contrast, geologic evidence of tsunami deposits and seismic crustal deformation along the Pacific coast of eastern Hokkaido indicate that the southern Kuril Trench has repeatedly ruptured during intervals of several hundred years, with the most recent event occurring in the 17th century (Nanayama et al., 2003; Sawai et al., 2004, 2009; Kelsey et al., 2006; Sawai, 2020). Therefore, another rupture is speculated to occur in the near future, as ~400 years have passed since the 17th-century earthquake (Sawai, 2020). Based on the evidence of tsunami deposits from the 17th century, which have been found at many sites in eastern Hokkaido and tsunami numerical simulations suggest that this earthquake was of Mw 8.8 or greater (Nanayama et al., 2003; Ioki & Tanioka, 2016). However, there is no information regarding the paleo-tsunami in the Pacific coast of southern Hokkaido, and clarifying the magnitude of Mw>8 earthquakes are a major issue. More than 17 sand layers have been reported to occur over several thousand years (Nanayama et al., 2003; Sawai et al., 2009). Some of these sand layers induced by of “unusually large” earthquakes-generated tsunamis, such as the 17th-century one, which could not explained by the observed tsunamis. For events prior to the 17th century, chronological correlations have rarely been examined, but accurate correlations of these tsunami records are important for understanding the recurrence intervals and rupture modes of megathrust earthquakes.

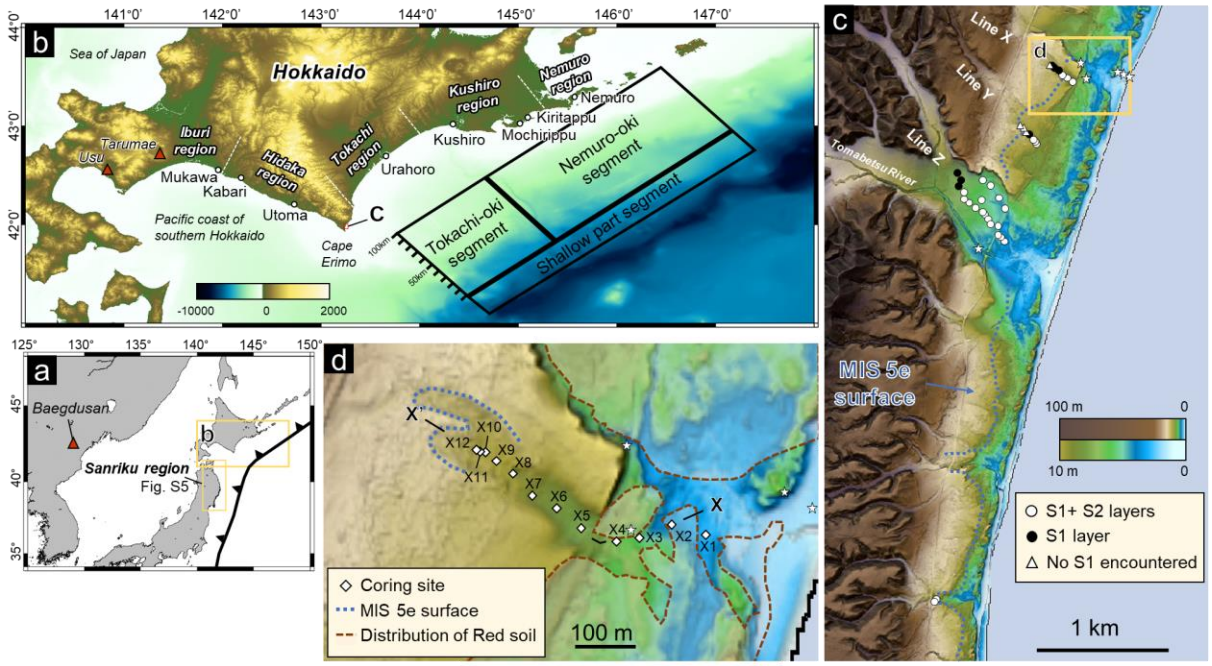

Figure 1. Study area. a: Location map of Hokkaido and Baegdusan. The black barbed line indicates the Pacific Plate subduction zone. b: Bathymetric and topographic map of Hokkaido. Paleotsunami investigation sites and local sources of tephra described by Nakanishi et al. (2020b) are marked. Black boxes indicate the 17th-century earthquake fault model area (Ioki & Tanioka, 2016). c: Topographic map based on 5 m-grid digital elevation model data from the Erimo area. Circles and triangles indicate location of coring sites. Also, circles show the distribution of S1 and S2. Blue dashed lines indicate the distribution of the MIS 5e surface (Koike & Machida, 2001). Stars indicate sand sampling locations for beach, river, and Red soil. The yellow box indicates the range shown in Fig. 1d. d: Close-up map of the coring sites on line X. The distribution of Red soil in 1947 is shown, as interpreted from aerial photographs. The stars are the same as in Fig. 1c.

In this study, we investigated the east coast of Erimo Cape to identify tsunami deposits and to estimate its spatial distribution. We estimated the wave source of the 17th century tsunami deposits newly discovered in this area using numerical simulations. The tsunami deposits are correlated with the event layers in the surrounding regions where the its ages have already been reported based on ^{14}C dating and tephrochronology. Based on the similarities and differences of the tsunami ages revealed by the event correlations in the coast along the Kuril Trench, this study discusses the tsunami history and coastal extent for the last 4,000 years from the Tokachi to Hidaka regions.

2 Background

2.1 Tectonic setting

The Pacific plate is subducting under the Okhotsk plate along the Kuril Trench at an average rate of ~8 cm/year (e.g., Sella et al., 2002). Instrumentally recorded earthquakes in the southern part of the Kuril subduction zone are known to occur at a magnitude of Mw7–8 with a fault length of ~100 km and a maximum value of 200 km (Satake, 2015). The rupture zone is classified into two segments, Tokachi-oki and Nemuro-oki, with a recurrence interval of 50–100 years (Satake, 2015). The interseismic GPS data and the seismic wave velocity studies suggest a gap in the asperity distribution in these rupture zones (Hashimoto et al., 2009; Liu et al., 2013).

2.2 Historical tsunami records

The most recent disastrous damaging earthquake in the southern Kuril Trench was the 2003 Tokachi-oki earthquake (Mw 8.0), recording and at the maximum tsunami generated wave height of the tsunami generated was 4 m (Tanioka et al., 2004). Although this tsunami caused traces a debris and minimal erosion of up to 3.5 m, which were reported in Erimo of Hokkaido, but no sandy deposits were formed (Nishimura et al., 2004). Earlier historical tsunamis originating from the Kuril and Japan Trenches have had recorded wave heights ranging of 3–4 m along the Erimo coast. However, there are no significant sandy deposits have been identified records of significant sandy deposits (Nakanishi et al., 2020a).

2.3 Previous work on geological records of tsunami

Since there are no historical records for Hokkaido before the 19th century (Satake, 2015), geological investigations of tsunami deposits and seismic crustal deformations have been reported (Nanayama et al., 2003; Sawai et al., 2004, 2009; Kelsey et al., 2006; Szczuciński et al., 2016; Ishizawa et al., 2017; Nakanishi et al., 2020a). In the Tokachi to Nemuro region, extensive tsunami deposit surveys have been carried out (Nanayama et al., 2003). Based on tephrostratigraphic correlation, previous studies have identified two sand layers between the 17th and 10th centuries, and 2–4 sand layers have been identified to be formed between 1000 and 2400 years ago. However, the detailed correlation between these sand layers is unclear due to the lack of comprehensive radiocarbon data (Sawai, 2020). The tsunami history of Harutoriko in the Kushiro region along with Kiritappu and Mochirippu area have been investigated based on wide-spread tephra and radiocarbon dating of tsunami deposits for the past 7,000 years (Nanayama et al., 2003, 2007; Sawai et al., 2009). However, comparison of ages for these regions is difficult because of large errors in the obtained ages. Precise radiocarbon dating has been reported for tsunami deposits for the past 3000 years in Urahoro, Tokachi region (Ishizawa et al., 2017), which is located ~100 km from Erimo. The tsunami deposits in eastern Hokkaido have anomalous distribution heights and extents that could not be deposited by tsunamis caused from earthquakes with Mw~8, such as the 1952 and 2003 Tokachi-oki earthquakes (Nanayama et al.,

2003, 2007; Sawai et al., 2009). Therefore this suggests that these deposits were deposited due to tsunamis from Mw~9 earthquakes that occurred in the rupture zone over Tokachi-oki and Nemuro-oki segments.

2.4 Regional setting

The east coast of Cape Erimo, Hokkaido, is located at the southern end of the Hidaka region and faces the Tokachi-oki segment (Fig. 1). This coast contains an ~200 m wide sandy beach where the maximum dune height is ~10 m above present sea level (asl). The first recorded mass settlement in this area was in 1872. Desertification of the area had progressed due to deforestation until a greening project was initiated in 1953 (Sakuraba, 2019). The aerial photographs taken in 1947 display that the coast was originally covered with an aeolian redeposited volcanic ashy material called "Red soil" for over 500 m length. (Fig. 1). Based on glacio-hydro isostatic adjustment (GIA) models, the relative sea-level change due to the GIA over the past 6000 years in the Erimo area was estimated as 0 ± 1 m (Okuno et al., 2014). Marine terraces during marine isotope stage (MIS) 5e extend parallel to the coast at ~15–25 m asl (Koike & Machida, 2001). The uplift rate is 0.02–0.17 mm/yr based on MIS 5e terraces on the Erimo coast when the GIA estimation of 125-ka is considered (Okuno et al., 2014). The Erimo coast is microtidal area where the maximum tidal range is < 1 m and the difference between the mean sea level and a mean higher high water is ~0.4 m (J-DOSS: https://www.jodc.go.jp/jodcweb/JDOSS/index.html). We surveyed the wetlands along lines X and Y (Fig. 1), which traverses depressions on the marine terraces. The depression perpendicular to the coastline on the marine terrace is considered to be the old river traces. The river topography is flat on the terrace surface of MIS 5e indicates that the rivers ceased to flow before at least 125 ka. Lines X and Y are part of an area that has been banned from exploitation due to the existence of the nature park since 1981. The line Z is parallel to the Tomabetsu River and this area is covered by a thick peat layer. The inland area was not surveyed due to the construction of residential areas.

3 Methods

3.1 Field surveys

Field surveys were conducted in October 2019, July 2020, and October 2020. Core samples were obtained from three survey lines (43 sites) to investigate the spatial distribution of tsunami deposits, especially those after the 10^{th} century. The samples were extracted using a handy Geoslicer (length of either 0.6 m: Takada et al., 2002) and a peat sampler (diameter of 7 cm, length of 2.5 m). We sampled the pre-10^{th}-century sediments to a depth of 1–2.5 m to investigate change of the sand layers inland on line X. The core samples were described sedimentary facies (color, grain size, thickness, bedforms) and photographed. Thereafter, the whole cores were transfer to a plastic case and subsampled in the laboratory for each laboratory analysis. Beaches, rivers, and aeolian sand (Red soil) around the peatland were collected to

examine the source of the sand layers (Fig. 1). The elevation profile of survey line X was measured via real-time kinematic positioning using Global Navigation Satellite System multi-band receivers (GNSS: ZED-F9P U-blox). The data pertaining to forests, where signal reception was not consistent, were supplemented by correcting the Digital Elevation Model (DEM: https://fgd.gsi.go.jp/download/menu.php) data of the Geographical Survey Institute (GSI) to ensure data matching, with respect to the GNSS data.

3.2 X-ray diffraction analysis

Since the mineral combinations in detritus reflect differences in sources and sedimentation (Jagodziński et al., 2009, 2012; Nakamura et al., 2012), X-ray diffractometry (XRD) analysis was conducted to identify the mineral species present in the sand layers. Since it is reported that onshore sand was dominant in modern tsunami deposits (e.g., Jagodziński et al., 2012; Nakamura et al., 2012; Szczuciński et al., 2012), beach and dune sand was considered as a candidate for the source of tsunami deposits. In addition, river sand from floods and aeolian sand were also considered, and these were analyzed and compared with the sand layers. 23 sand and mud samples were collected from the core samples and the source candidate sand sampled from the sampling sites are shown in Fig. 1. In all sand samples, the medium grain sample was used. We also analyzed the very fine grain sample for checking grain size effect. The mineralogical composition was determined by XRD (Bruker D2 PHASER) performed by the same method described in Nakanishi et al. (2020a). The conditions for analysis were set at 30 kV, 10 mA, 0.02 steps for 1 s, and a registration 2θ range from 5° to 65°.

3.3 Grain size analysis

The grain size distribution of a sand layer is widely used to determine its origin and transport mode (e.g., Folk & Ward, 1957; Morton et al., 2007). We performed grain size analysis using a sieve on each sand layer obtained from the cores and the surrounding sand (beaches, river, and aeolian sand). We sampled 26 samples in total, at every 1 cm in the vertical direction at X5 site and from the bulk layer at other sites. Samples of 10–20 g were pretreated with H_2O_2 to remove the organic matter and disperse the particles. The dried samples were sieved using a set of 14 sieves with mesh sizes ranging from 4.5 phi to -2.0 phi. Basic statistics such as mean (Mz), standard deviation (σ_I), and skewness (Sk_I) were calculated following the method outlined in Folk & Ward (1957).

3.4 Radiocarbon dating

Radiocarbon dating was used to determine the depositional age of the tsunami deposits (Table 1). Analytical samples (units of 1 cm) were collected above and below the sand layers as plant fragments in peat, avoiding roots. When plant fragments were not available, bulk samples were used for measurements. Graphitization of the sample was performed via the same method employed by Nakanishi et al. (2020a), and ^{14}C dating was prepared at the Atmosphere and Ocean

Research Institute using Single Stage accelerator mass spectrometry (Yokoyama et al., 2019). We calibrated the ^{14}C ages to the calendar ages using the OxCal 4.4 with the IntCal20 dataset (Reimer et al., 2020). The P_Sequence and Sequence model and the general outlier model in OxCal were used to constrain the calibration ages using stratigraphic order (Bronk Ramsey, 2008, 2009a, 2009b). Each model was constructed separately for individual peat layers among the tsunami deposits (Ishizawa et al., 2017, 2020). The recurrence intervals of tsunamis were estimated from the age difference between each sand layer (Lienkaemper & Bronk Ramsey, 2009). We re-calibrated the ^{14}C age of the reported tsunami deposits using the same protocols (Ishizawa et al., 2017; Nakanishi et al., 2020a) using IntCal20.

Table 1. ^{14}C dating results.

Sample name	Material	Site	Depth (cm)	^{14}C age	Error	Modelled age (1σ) from	Modelled age (1σ) to	Modelled age (2σ) from	Modelled age (2σ) to	Mean	Lab number
peat-S1_2U	Bulk peat	X5	-30	392	±25	500	461	511	335	469	YAUT-053023
peat-S1_2L	Bulk peat	X5	-35	814	±24	714	683	733	677	702	YAUT-053019
peat-S2L	Bulk peat	X5	-41	862	±22	776	732	897	725	766	YAUT-053018
peat-S5U	Bulk peat	X5	-54	1475	±24	1379	1315	1393	1307	1352	YAUT-053017
peat-S5_6U	Bulk peat	X5	-60	1801	±26	1728	1630	1780	1608	1684	YAUT-053016
peat-S5_6L	Bulk peat	X5	-66	1971	±24	1925	1838	1977	1827	1888	YAUT-053015
peat-S6_7U	Bulk peat	X5	-70	2053	±27	2051	1950	2098	1940	2012	YAUT-053013
peat-S6_7L	Bulk peat	X5	-71	2119	±23	2120	2048	2145	2004	2082	YAUT-053012
peat-S7L	Plant fragment	X5	-78	2304	±25	2350	2324	2358	2182	2322	YAUT-053011
peat-S8U	Plant fragment	X5	-83	2524	±23	2719	2515	2732	2492	2587	YAUT-053009
peat-S8_9U	Plant fragment	X5	-100	2679	±24	2841	2755	2850	2750	2792	YAUT-053006
peat-S8_9L	Plant fragment	X5	-106	3010	±26	3240	3156	3331	3075	3198	YAUT-053005
peat-S9_10U	Plant fragment	X5	-112	3216	±25	3460	3401	3480	3379	3428	YAUT-053004
peat-S9_10L	Plant fragment	X5	-115	3411	±24	3672	3578	3703	3568	3631	YAUT-053003
peat-S10L	Plant fragment	X5	-121	3563	±25	3897	3833	3969	3728	3863	YAUT-053002

Sample name	Material	Site	Depth (cm)	^{14}C age	Error	Calibrated age (1σ) from	Calibrated age (1σ) to	Calibrated age (2σ) from	Calibrated age (2σ) to		
peat-209cm	Plant fragment	X4	-195	3628	25	3976	3900	4071	3849	3942	YAUT-053024

3.5 Numerical simulation

To estimate the origin of the sandy layers in this area, tsunami numerical simulations were carried out using the source faults of the 17th-century earthquake based on the distribution of tsunami deposits (Satake et al., 2008; Ioki & Tanioka, 2016). The numerical simulations were performed using the tsunami calculation code "JAGRUS" (Baba et al., 2015, 2017). We used the bathymetric data from the Japan Oceanographic Data Center and the M7000 series from the Japan Hydrographic Association. The ASTER GDEM Version 3 from Shuttle Radar Topography Mission (https://doi.org/10.5067/ASTER/ASTGTM.003) and the 5-m mesh DEM data from the GSI were used as topographical data. In order to avoid underestimating the inundation area, the

modern roads that are assumed not to have existed in the 17th century were manually cut out and flattened using the surface command of generic mapping tools (Wessel et al., 2013). We nested the geographical data in the following order of 450 m, 150 m, 50 m, 16 m, and 5 m grid size. The calculations were carried out using a linear long-wave equations for the 450 m grid size system and a non-linear long-wave equations for the finer grid size systems in a staggered-grid, leap-frog finite differential scheme. The absorbing boundary condition was applied at the edge of the computational domain. The time step was 0.1 s to safety reach a stability condition. Manning's roughness coefficient was 0.03 $m^{-1/3}s$ as per Ioki & Tanioka (2016). The tide level was assumed to be constant at the present mean sea level. The seismic deformation was computed as per the formula of Okada (1985), and the rise time was assumed to be 60 s (the deformation was included in the geographical data). The tsunami propagation calculations were performed up to 7200 s.

4 Description of tsunami deposits

4.1 Stratigraphy and depositional ages

The sedimentary sequence on line X, from bottom to top, was as follows: fibrous dark brown peat or a clay layer, black peat intercalated by gray sand layers, reddish-brown soil or sand as "Red soil", and topsoil. The clay layer was observed to be pinkish-brown to yellowish-brown sticky clay at depths of ~0.5 m or more from the ground surface on the landward side of the X6 site (Figs. 2 and S1). On the seaward side of the X5 site, a fibrous peat layer was observed below ~1.5 m from the ground surface. Here, the sand layers were either thinner than 5 cm thick, or no sand layer was observed.

Three tephra layers and ten sand layers were intercalated in the black peat. The tephra layers have already been identified in this area by Nakanishi et al. (2020b), from top to bottom as follows: a patchy white volcanic ash layer (1663 AD, Usu Volcano-b tephra: Us-b), a yellowish-white volcanic ash layer with a thickness of ~2 cm (946 AD, Baegdusan Volcano-Tomakomai tephra: B-Tm), and an orange volcanic ash layer with a patchy 2-cm thickness within the peat layers (~2400 BP, Tarumae Volcano-c2 tephra: Ta-c2). We observed two sand layers between the Us-b and B-Tm tephra, five sand layers between the B-Tm and Ta-c2 tephra, and three to five sand layers below the Ta-c2 tephra (named S1–10 from top to bottom). In the age-depth model, the depositional ages obtained from the peat layers by ^{14}C dating and the tephras were linearly correlated (Fig. 3). This model is also consistent with the known ages of the volcanic ash layers. The depositional rate was constant (0.14 mm/yr), indicating continuous deposition of the peat layers. The most basal sand layer (i.e., S10) was deposited after 3900 BP.

A reddish-brown sand layer and soil was found as "Red soil" in sets around the ground surface. The reddish-brown sand layer have a mode of 1.5 phi with poor sorting and a high background and a low mineral peak intensity of XRD (Figs. 4, 5, S2 and, S3), indicating rich amorphous components such as a pumice. Therefore, the reddish-brown sand layers can be

distinguished from gray sand layers by the fact that they are found only near the ground surface, are poor poorly sorting, and contain pumice. The topsoil is black and consists of litters, which changes gradually to Red soil. Core samples from other sites along line X are consisted of black

or fibrous peat. Two gray sand layers (S1 and S2) were identified in the peat layers between Us-b and B-Tm in each survey line.

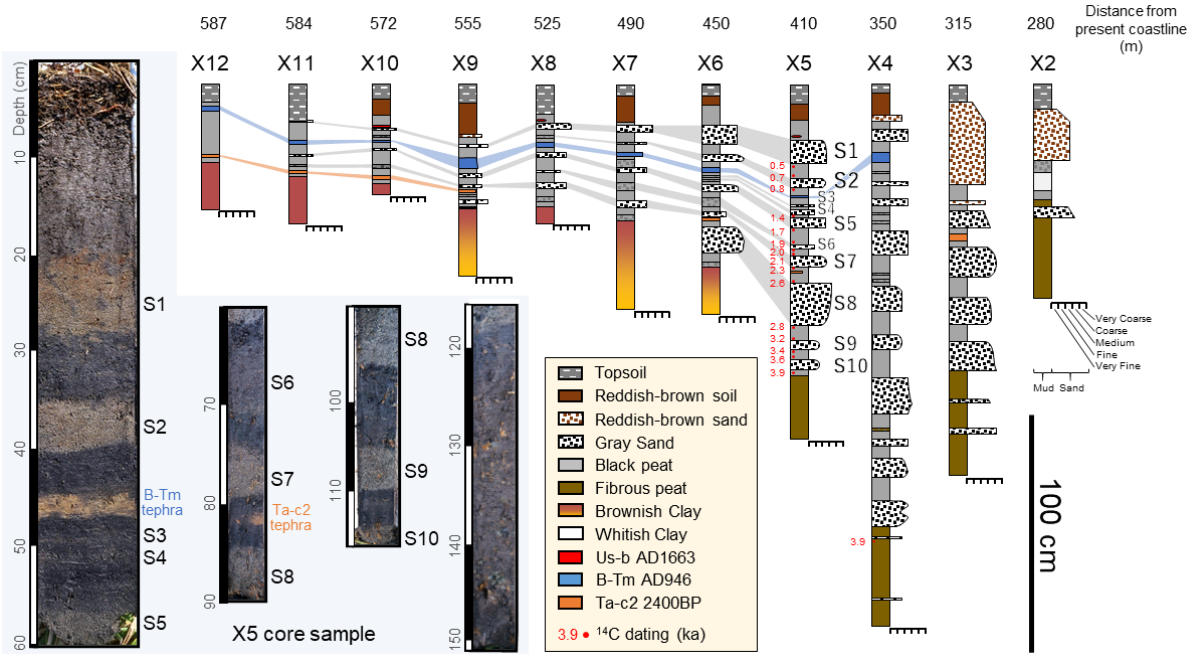

Figure 2. Correlated stratigraphic columns along survey line X and photographs of the core samples from the site X5.

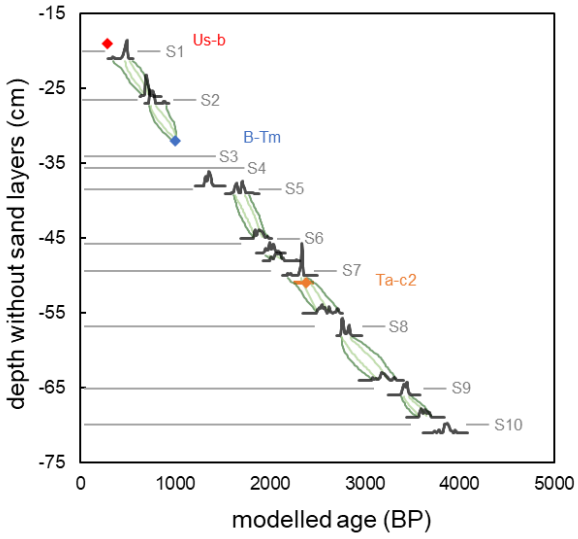

Figure 3. Age-depth model without the sand layers at the site X5. Black histograms show modelled ^{14}C age (Table 1). The dark and light green lines indicate the range of 2σ and 1σ modelled ages, respectively. Red and blue diamond's indicate widespread tephra (Us-b: 1663 AD, B-Tm: 946 AD) with incorporated into the age-

depth model. Yellow diamond and bar indicate Ta-c2 median ages and 2σ range calculated by the same method as the event layers, respectively.

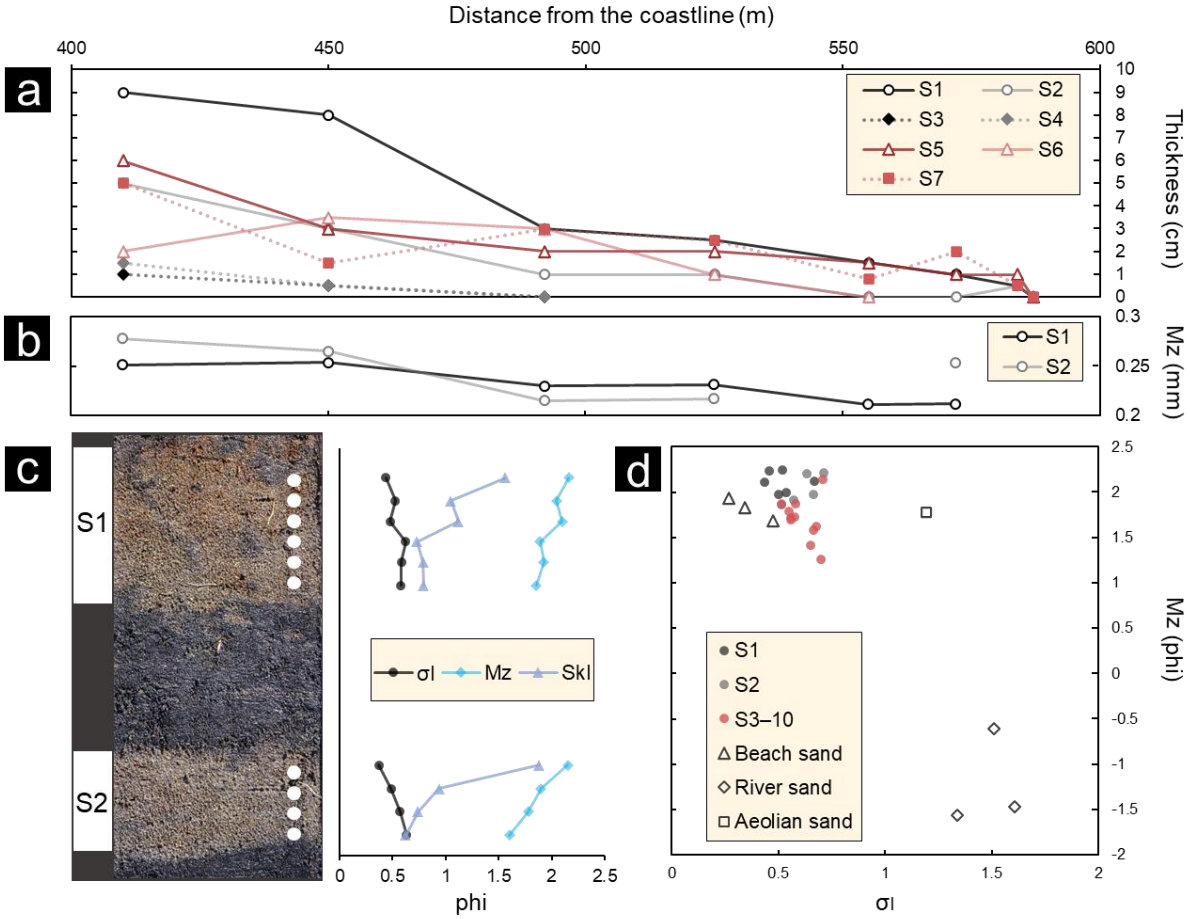

Figure 4. Layer thickness and grain size analysis results for S1–10 and source candidate sand. a: Thickness change of S1–7 on line X. b: Horizontal changes of the mean diameter of S1 and S2 on line X. c: Vertical

changes of the mean diameter (Mz), standard deviation (σ_I), and skewness (Sk_I) for S1 and S2. d: Scatter plot of mean diameter and standard deviation in S1–10 of line X, beach, river and aeolian sand (Red soil).

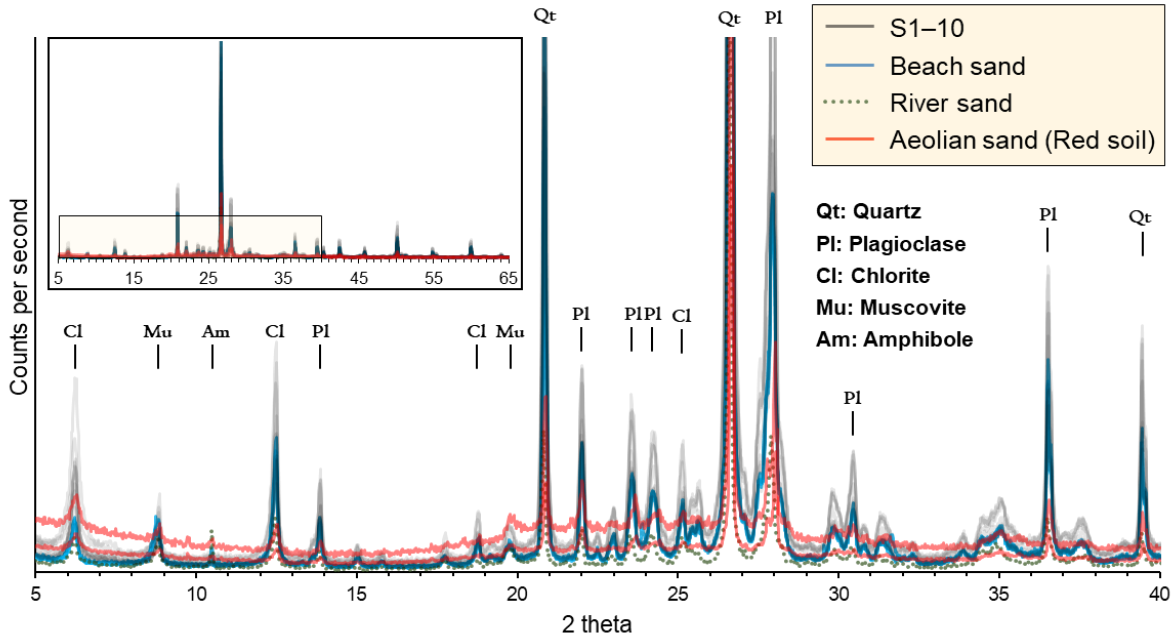

Figure 5. Results of mineralogy analysis using XRD for S1–10 at the site X5 (10 samples), beach sand (3 samples), river sand (1 sample) and, Red soil (2 samples). The inserted figure shows the whole view and the zoomed-out part.

4.2 Sand layer characteristics

S1–10 were observed to be homogeneous and well-moderately well sorted fine to medium sand (Fig. 4). These sand layers commonly indicated single normal grading and sharp basal contacts. Some of thick sand layers contained rip-up clasts of black peat (Fig. S4). S1–8 exhibited a mode of 2.5 phi and demonstrate very positive skewness. The grain size composition of S9 and S10 were consist of 0.5–2.5 phi and moderately well sorted sand on X5 (Fig. S2). The mineral assemblages of S1–10 were mainly quartz, feldspar, and chlorite, with low background value, indicating no amorphous components (Fig. 5). Mineral assemblages did not vary significantly with sample grain size or distance from the coastline. The mineral assemblages of beach and river sands are similar to those of S1–10, but the river sand differ from S1–10 in that that it has a higher proportion of hornblende and a lower proportion of other minerals.

The correlation between the cores was estimated based on the tephras and the thickness of the peat layers. The black peat layer exhibited a constant sedimentation rate as shown by the age-depth model (Fig. 3), therefore, its thickness was assumed to be proportional to its accumulation age. Between Us-b and B-Tm, S2 changes to sandy peat at a site inland from X8,

and could not be identified further. Since only a single layer of sand was deposited 8 cm above B-Tm (the interval is ~600 yr), S1 was distributed at least till X11. Between B-Tm and Ta-c2, S3, S4, and S6 were < 2 cm layers and could not be identified until the X8 site. Two sand layers were identified from X9 to X11. Therefore, these could be compared with S5 and S7 based on the thickness of the peat layer (~2.5–4 cm below B-Tm and ~1–2 cm above Ta-c2 indicate ~1200–1300 BP and ~2400–2100 BP, respectively). The sand layers below Ta-c2 were difficult to compare because of limited dating, but S8–10 were likely comparable because of the presence of three or more sand layers on the seaward and landward sides. S1–7 exhibited a sheet distribution up to 450–600 m inland (up to 7–11 m asl) on line X (Figs. 4 and 6). The thickness of S1–7 exhibited a trend of gradual thinning inland; eventually, the sand layers became sandy peat or unrecognizable. S1, S5, and S7 were relatively thick and could be identified farthest inland (up to X11). In contrast, S3 and S4 were recognized as thin sand layers at X4, and their distribution was limited to 450 m from the shoreline. We focused on S1 and S2 to clarify their distribution in a wide area of the Erimo coast (Figs. 1 and 6). The distribution could be observed along the coast for several kilometers, and inland over 1 km along line Z, where the topography was relatively gentle. S1 was distributed further inland than S2 along all survey lines (Fig. 1). S1 and S2 indicated that grain size gradually fines inland, from medium to fine sand (Fig. 4).

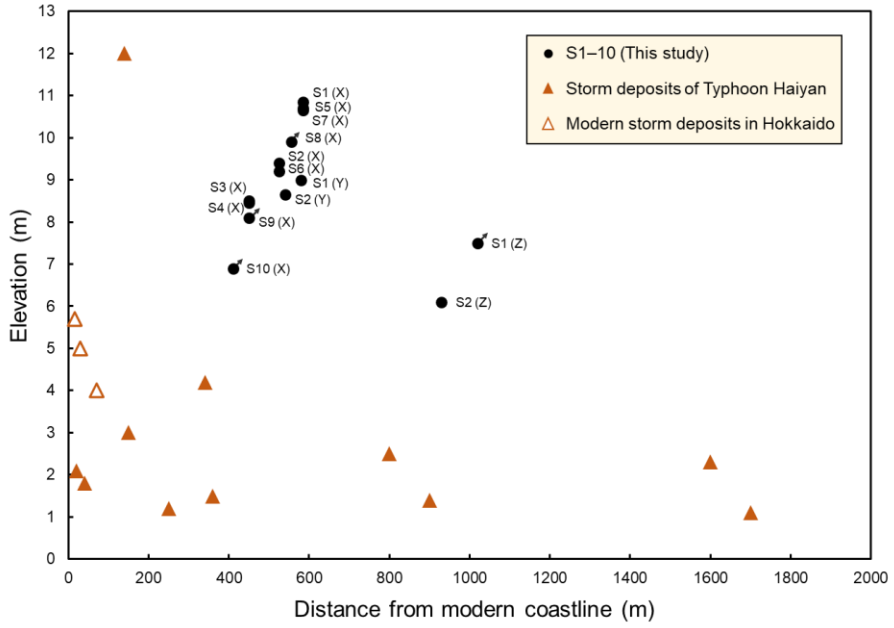

Figure 6. Distribution heights and distances from the present coastline of S1–10 on each survey line. Black plots with arrows indicate sand layers that are potentially distributed farther inland due to unconfirmed distribution limits. The alphabets in parentheses indicate the name of the survey lines. Filled and white triangles indicate the maximum distribution of the storm deposits of Typhoon Haiyan in the central Philippine coast and the modern storm deposits reported in Hokkaido, respectively (Brill et al., 2016; Soria et al., 2017, 2018; Nishimura & Miyaji, 1996; Ganzei et al., 2010; Shigeno & Nanayama, 2016; Chiba & Nishimura, 2018;

Switzer et al., 2020). The data from Typhoon Haiyan is used for comparison as a largest storm, not as the one that actually affected Hokkaido.

4.3 Interpretation of formation of anomalous sand layers

S1–10 were observed in the peat with a sharply boundary with the rip-up clasts. The sand layers show the single normal grading structure and the fine-grained trend inland. The grain size compositions of S1–10 were similar to those of the beach and dune sand, and were distinguished from poorly sorted aeolian sand and coarse-grained river sand (Figs. 4 and 5). The mineral assemblages also support the fact that beach sand is the major source of S1–10. It is unlikely that S1–10 were transported by river floods because the sediments of nearby rivers are gravel (Fig. 4). An aeolian sand such as Red soil is distinguished from S1–10 by the presence of amorphous pumice and the poorly sorted sand. In addition, the repetition of the sharp contrasts between the peat and the sand layers with the rip-up clasts can only have been formed by an abrupt event such as an extreme wave.

Tsunamis and storms surge are known to form sand layers beyond the back-barrier (e.g., Morton et al., 2007; Takashimizu et al., 2012; Brill et al., 2016). In general, even though extreme waves from storms show high inundation heights, the distribution of a sand layer is often limited around a beach area (Morton et al., 2007; Watanabe et al., 2018). A storm surge is also a gradual rise in water level, inundating the beach from lowest points. thus, a distribution of storm deposits is often scattered and lobe-shaped (Nishimura & Miyaji, 1996; Brill et al., 2016; Chiba & Nishimura, 2018). Storm deposits have also been reported in Hokkaido, and their distribution was reported up to 4–6 m asl and a few tens of meters from the shoreline (Nishimura & Miyaji, 1996; Ganzei et al., 2010; Shigeno & Nanayama, 2016; Chiba & Nishimura, 2018; Switzer et al., 2020). Additionally, tsunamis result in erosion and inland transportation of a large volume of sediments in a short time interval (Morton et al., 2007; Szczuciński et al., 2012; Goto et al., 2014). As a result of erosion, the contact between the transported sand layer and the background sediment indicates very sharp and often observed rip-up clasts (Szczuciński et al., 2012; Takashimizu et al., 2012). The inundation flow is slowed by flooding on land, and the grains with higher specific gravity settle and are eventually recorded in the sediment as grading structures (Jaffe et al., 2012; Yoshii et al., 2017). The amount of transported sediments is limited owing to the decrease in tsunami flow velocity and inundation depth; thus, sheet-like distribution and gradual thinning are observed (Szczuciński et al., 2012; Takashimizu et al., 2012; Goto et al., 2014).

S1–10 exhibited normal grading and a sharp basal contact with rip-up clasts; these sedimentary structures indicate an erosional flow and decrease in velocity of single flows. The distribution extended several hundred meters inland from the beach and in a wide area along the shoreline. In addition, the elevation of the sand layer distribution is at least 7–11 m asl, which is

significantly higher than that of the modern storm deposits (Fig. 6: Brill et al., 2016; Soria et al., 2017, 2018; Nishimura & Miyaji, 1996; Ganzei et al., 2010; Shigeno & Nanayama, 2016; Chiba and Nishimura, 2018; Switzer et al., 2020). The elevation of the deposits is more than 5 m asl even considering the relative sea level of the past 4000 years based on the hydro-isostasy and the crustal uplift (up to +2.1 m at mean higher high water level: Koike & Machida; Okuno et al., 2014). For the past 4000 years, the Erimo coast has been limited to the area ~100 m from the present coastline with elevations under 2 m asl. Therefore, the distribution of S1–10 along line X is estimated more than 300–500 m from the past coastline. Considering that the distribution of S1–10 cannot be explained by anomalous storms and some sedimentary structures are common to tsunami deposits, these are interpreted as anomalous sand layers deposited by high tsunami waves.

5 Numerical simulations

The tsunamis induced by the Mw~8 earthquakes of the Kuril Trench are known to have a recurrence period of several decades (e.g., the 1952 and 2003 Tokachi-oki earthquake). Given that no sandy deposits have been transported into the back-barrier by these tsunamis (Nishimura et al., 2004), it is unlikely that tsunamis induced by the Mw~8 earthquakes transported the S1–10 tsunami deposits. Therefore, we used numerical simulations to reconstruct the tsunami inundation height resulting from a Mw~9 earthquake. A source rupture model based on geological data has been proposed for 17th-century earthquakes (Nanayama et al., 2003; Satake et al., 2008; Ioki & Tanioka, 2016). The T10N5S25 model (Mw 8.8: T10 means 10 m slip on Tokachi-oki segments, N5 means 5 m slip on Nemuro segments, S25 means 25 m slip on the shallow part segment; Fig. 1) reproduces an inundation area that covered distribution of tsunami deposits extending from the Tokachi to Nemuro regions (Ioki & Tanioka, 2016). In addition to the distribution of tsunami deposits, these source rupture models are required to meet the constraint that the tsunami wave height should not exceed 3 m in the Sanriku region because there is no description of an earthquake like this in the historical documents (Satake et al., 2008). However, this requirement has not yet been appropriately fulfilled.

We tested whether the T10N5S25 model can be applied to the 17th-century tsunami deposits in the Erimo area, further to the west. The resulting inundation area did not cover the entire distribution of S1 (Fig. 7). In order to not affect the tsunami simulation results from the Tokachi to Nemuro regions, we attempted to adjust the fault model to expand the tsunami inundation area in the Erimo area. If, in the Tokachi-oki segment, the rupture model parameter is made wider, or the slip amount is increased, the maximum wave height along the Sanriku coast will be higher. Therefore, we attempted to reproduce the inundation area in Erimo by narrowing the fault width, as it is known that wavelength affects the extent of inundation depending on the topography (Satake et al., 2013). The fault widths were set every 10 km, ranging over 40–90 km

(T10w40–T10w90) along the Tokachi-oki segment; N5 and S25 are constant in all conditions. The magnitude of these rupture models were Mw 8.7–8.8.

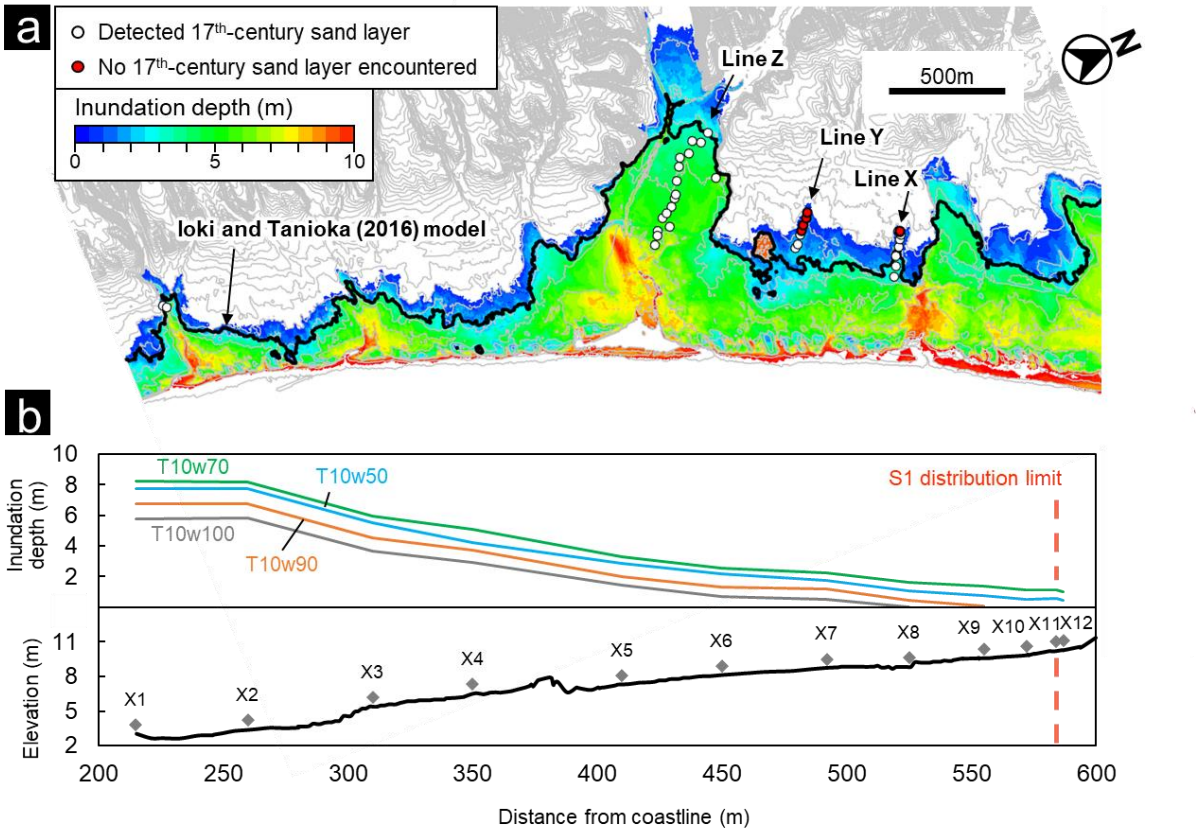

Figure 7. Simulation results of tsunami run-ups in the Erimo coast. a: Tsunami inundation area using the Ioki & Tanioka (2016) model (Black line) and the T10w70 model (colored). b: Tsunami inundation depth profiles for each fault width condition and topographic profile on line X. T10w100 is conventional model (Ioki & Tanioka, 2016)

The T10w50–T10w70 models produced an inundation area that covered the entire distribution of S1 (Fig. 7). These models also changed the energy-directivity to the Sanriku region, such that the maximum wave heights on the Sanriku coastline decreased as the fault width narrowed (Fig. S5). The maximum wave heights on the coastline from the Tokachi to Nemuro regions also exhibited a slight decrease when narrow fault width conditions were applied. The T10w70 model is more reasonable because it reproduces an inundation area that covers enough tsunami deposits and minimizes the change in wave height from the Tokachi to Nemuro regions.

The crustal deformation of this model exhibits subsidence of ~15 cm around Erimo (Fig. S6), while the model proposed by Ioki & Tanioka (2016) exhibited a subsidence of ~40 cm, which does not explain the difference in the extent of inundation. Locally high wave heights in the Erimo area likely reflected shortening of the wave periods, caused by narrowing of the fault

width. When the fault width of T10 is 100 km, there is a certain interval between the first and second waves, but the T10w70 model shows that the first wave propagates slightly slower and excites the second wave (Fig. 8). In addition, in the T10w70 model, the third wave appears earlier and merges with the wave trapped by the shallow bathymetry on the Erimo Cape extension, expanding the inundation area subsequent to the second wave. The landward side of X5 was inundated only by the first wave (Fig. 8). This is consistent with the fact that the observed sedimentary structure of the sand layers was single normal grading (Fig. 4). The T10w70 model is almost equal to Mw 8.8, which is the same scale as the conventional model. This means that the model based on the tsunami deposits from the Tokachi to Nemuro regions can reproduce the distribution of tsunami deposits found in the western end of the eastern Hokkaido coast, without major changes. In this numerical simulation, we used a simple modification method, involving changing the fault width of the Tokachi-oki segment, however, it is known that an actual rupture zone is not rectangular but heterogeneous (e.g., Liu et al., 2013). By taking this into account, a simulation could reproduce the distribution of tsunami deposits in each region with greater accuracy. On the other hand, it should be noted that the distribution of preserved sand layers contains uncertainties because tsunami sediments are known to be remigrated by post-depositional proccess (Richmond et al., 2012; Szczuciński, 2020). In order to reduce such an uncertainty, it is necessary to evaluate the tsunami inundation area by using

456 chemical and biomarker methods independent of the sand layer (e.g., Szczuciński et al., 2016;
457 Chagué-Goff et al., 2017).

458

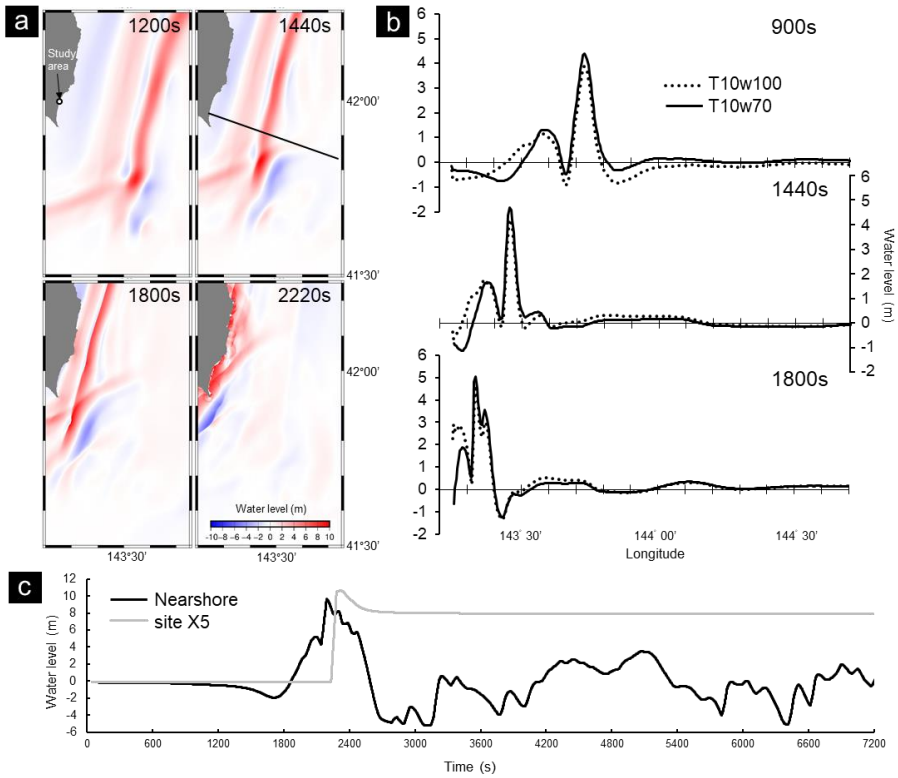

459

460 Figure 8. Tsunami waveform on the time series from the numerical simulation of the 17th-century tsunami. a:
461 Temporal changes in water level for the T10w70 model. Snapshots taken at 1200, 1440, 1800, and 2220
462 seconds after the earthquake. Black line shows survey line from Figure 8b. b: The wave profiles on the black
463 line of Fig. 8a at 900, 1440, and 1800 seconds for T10w100 and T10w70 models. c: Time series of tsunami
464 waveforms of T10w70 model at site X5 and nearshore of line X. The elevation in DEM at the site X5 is 7.9 m
465 asl.

466

467 **6 Correlation of tsunami deposits**

468 The recurrence intervals for layers S1–10 ranged from 110 to 620 years (Table S1). Such
469 tsunami recurrence intervals have been reported in the Tokachi and Hidaka regions (Ishizawa et
470 al., 2017; Nakanishi et al., 2020a). To verify whether these paleo-tsunamis were formed by
471 tsunamis of the same origin, we compared the depositional ages of the sand layers with those
472 reported for Urahoro and Utoma, which were measured using the same ^{14}C dating method (Fig.
473 9). The agreement on the probability density function of events obtained by the sequencing
474 model for each region was calculated using the overlapping coefficient (OVL: Inman & Bradley,

1989; Hutchinson & Clague, 2017: Table S2). Hutchinson & Clague (2017) adopted critical threshold values for probable coeval events when OVL was > 0.25. In the Erimo and Urahoro areas facing the Tokachi-oki segment, the depositional ages were comparable in all the observed sand layers, and OVL ranged from 0.39–0.78 (Table S2). In particular, S2 and L2 showed a narrow range from ~800 to 700 BP, with an error of 20 years. The results mean that Urahoro and Erimo were struck by the same number of large tsunamis at the same time during the past 3000 years. In the Utoma area, located on the southern Hidaka coast, the depositional ages were comparable in the four sand layers, except for U3, and OVL ranged from 0.26–0.81 (Table S2). The geological record in Utoma is currently limited to the period before 2000 BP, but the tsunamis with recurrence intervals of ~430 years are most likely to have been generated by Mw>8 earthquakes of the Kuril Trench. However, it is necessary to consider the possibility that tsunamis from different sources, such as the U3 event in Utoma, are also included in the data.

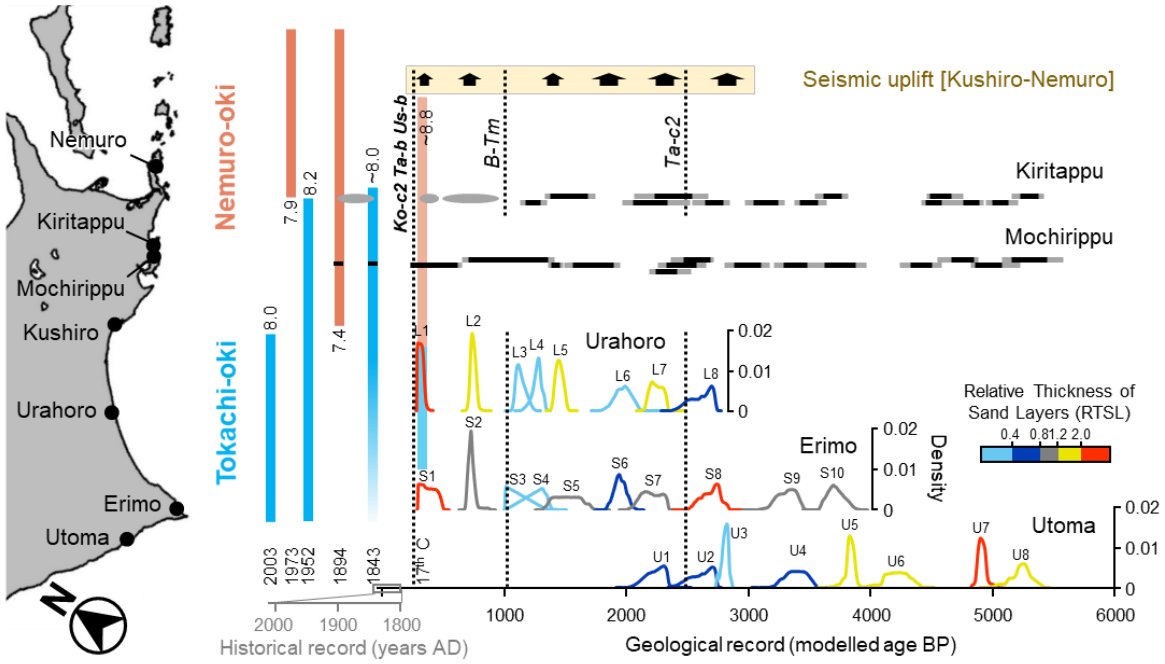

Figure 9. Depositional ages of the sand layers in the Hidaka and Tokachi regions (Ishizawa et al., 2017; Nakanishi et al., 2020a). The depositional ages are presented as the probability density function. The color scale of histogram indicates the relative thicknesses of the sand layer (RTSL). The RTSL were normalized using the median value and exclude any outliers. The outliers were set to exceed the interquartile range by 1.5 times based on the upper quartile. The gray and black bars indicate the estimated ages (2σ and 1σ, respectively) of tsunamis reported in the Mochirippu and Kiritappu areas (Sawai et al., 2009). Black arrows indicate the age range of the seismic uplift in the Kushiro to Nemuro regions (Kelsey et al., 2006). The blue and red color bars indicate the fault lengths of the earthquakes that occurred off the Tokachi and Nemuro

coast, respectively (Satake, 2015). The number beside each color bar indicates the moment magnitude of the earthquake.

The relative thicknesses of the sand layers (RTSL), normalized by the median values of all the sand layers within the core, were also shown with tsunami ages (Fig. 9). In Erimo and Urahoro, it is very interesting to match the patterns of the high and low values, except for layer S8. This good agreement between the two regions, in spite of the 100 km distance between them, may support the assumption that both regions suffered from tsunamis of similar magnitude. This is because modern tsunami deposit studies infer that the thickness of a tsunami deposit is most sensitive to the inundation depth (Goto et al., 2014; Naruse & Abe, 2017). However, it should be noted that microtopography, accommodation space, sediment source, and post-depositional changes all significantly influence on the thickness of the tsunami deposits (Szczuciński, 2020). Actually, the RTSL in Utoma is thick in the sand layers deposited around 5000 BP, which was due to the influence of the highstand sea-level in the mid-Holocene (Nakanishi et al., 2020a).

The distribution of the compared tsunami deposits along the coastline stretches at least 150 km, suggesting that they were caused by tsunamis resulting from Mw>8 earthquakes, with fault lengths of several hundred kilometers. Therefore, few of the S1–10 events are expected to be correlated with the geological evidence identified from the Kushiro to Nemuro regions for paleo-earthquakes (Nanayama et al., 2003; Sawai et al., 2004, 2009; Kelsey et al., 2006). The age of the tsunami and seismic crustal movement in Kiritappu and Mochirippu has been estimated based on ^{14}C dating (Sawai et al., 2009). However, direct correlation is difficult because of the difference in the sample materials, dating methods, and dating depth points. The number of sand layers between the Nemuro and Tokachi-Hidaka regions does not match, even if the correlation is simply based on tephrochronology. Thus, both regions likely experienced at least some differing paleo-tsunamis. The estimated ages of the seismic uplifts in the Nemuro to Kushiro region (Kelsey et al., 2006) seem to correlate with the depositional age of the relatively thick sand layers found in the Hidaka and Tokachi regions (e.g., S1, S5 and, S7). The distributions of layers S1, S5, and S7 in the Erimo area are the most extensive inland (Fig. 7). Thus, these tsunamis might have derived from larger magnitude earthquakes or wider rupture zones compared with other events in the Tokachi-Hidaka regions.

7 Conclusions

We found ten anomalous sand layers in the coastal wetland in Erimo, Hokkaido, Japan. These sand layers share similarities with beach sand and can be distinguished from aeolian and river sand. Moreover, they share common features with modern tsunami deposits, such as normal grading structure, and a sharp basal contact with rip-up clasts. The sand layers are distributed over several hundred meters from the shoreline (up to 7–11 m asl), which could not be explained by extreme storms or tsunamis caused by Mw~8 earthquakes. Numerical simulations were

performed for the 17th-century tsunami to examine whether the distributions of the 17th-century sand layer can be reproduced by the Mw8.8 earthquake model in the Tokachi to Nemuro segments. The results show that the distribution can be reproduced in the Erimo coast by slightly modifying the fault width of the conventional model. The correlation of the tsunami events in the past 4000 years is consistent with the tsunami evidence from the Tokachi and Hidaka region, and demonstrates recurrence intervals of 110–620 years. The chronological correlation between most tsunamis at these sites indicates that the paleo-tsunamis reported in eastern Hokkaido reached the Hidaka region. On the other hand, detailed study of the tsunami ages also revealed the differences among the regions facing the Tokachi-oki and Nemuro-oki segments, suggesting the diversity of the Kuril earthquakes every few hundred years. By extending the correlation of paleo-tsunamis from Hidaka to Tokachi to the past 4000 years, the spatial extent and recurrence interval of large tsunamis in the regions facing the Tokachi-oki segment have been significantly updated. The common history of tsunamis in the area facing the Tokachi-oki segment revealed by this study will provide a framework for a more comprehensive correlation of Mw>8 earthquakes in the entire Kuril Trench.

Acknowledgments

The authors would like to thank S. Ishikawa, from the Erimo town office, for allowing us to conduct field surveys. We appreciate the valuable comments by Y. Sawai and K. Ioki (AIST). This research was supported by Grant-in-Aid from the JSPS to R. Nakanishi (20J21239) and to Y. Yokoyama (20H00193).

Data Availability Statement

New ^{14}C datasets for this research are provided as Table 1 in this paper. We used tsunami calculation code JAGURS (Baba et al., 2015, 2017) at https://doi.org/10.5281/zenodo.3737816. Generic Mapping Tools was used to draw the figures (Wessel et al., 2013).

References

Baba, T., Takahashi, N., Kaneda, Y., Ando, K., Matsuoka, D., & Kato, T. (2015). Parallel Implementation of Dispersive Tsunami Wave Modeling with a Nesting Algorithm for the 2011 Tohoku Tsunami. Pure and Applied Geophysics, 172(12), 3455–3472. https://doi.org/10.1007/s00024-015-1049-2

Baba, T., Allgeyer, S., Hossen, J., Cummins, P. R., Tsushima, H., Imai, K., et al. (2017). Accurate numerical simulation of the far-field tsunami caused by the 2011 Tohoku earthquake, including the effects of Boussinesq dispersion, seawater density stratification, elastic loading, and gravitational potential change. Ocean Modelling, 111, 46–54. https://doi.org/10.1016/j.ocemod.2017.01.002

Brill, D., May, S. M., Engel, M., Reyes, M., Pint, A., Opitz, S., et al. (2016). Typhoon Haiyan's sedimentary record in coastal environments of the Philippines and its palaeotempestological implications. Natural Hazards and Earth System Sciences, 16(12), 2799–2822. https://doi.org/10.5194/nhess-16-2799-2016

569 Bronk Ramsey, C. (2008). Deposition models for chronological records. Quaternary Science Reviews, 27(1), 42–60.
570 https://doi.org/10.1016/j.quascirev.2007.01.019

571 Bronk Ramsey, C. (2009a). Bayesian Analysis of Radiocarbon Dates. Radiocarbon, 51(1), 337–360.
572 https://doi.org/10.1017/S0033822200033865

573 Bronk Ramsey, C. (2009b). Dealing with Outliers and Offsets in Radiocarbon Dating. Radiocarbon, 51(3), 1023–1045.
574 https://doi.org/10.1017/S0033822200034093

575 Chagué-Goff, C., Szczuciński, W., & Shinozaki, T. (2017). Applications of geochemistry in tsunami research: A review. Earth-
576 Science Reviews, 165, 203–244. https://doi.org/10.1016/j.earscirev.2016.12.003

577 Chiba, T., & Nishimura, Y. (2018). Depositional processes of the storm surge deposits due to Typhoon 1523 in Horokayanto,
578 Hokkaido, Japan. The Quaternary Research (Daiyonki kenkyu), 57, 53–63 (in Japanese, with English abstract).

579 Folk, R. L., & Ward, W. C. (1957). Brazos river bar: A study in the significance of grain size parameters. Journal of Sedimentary
580 Petrology, 27(1), 3–26. https://doi.org/10.1306/74D70646-2B21-11D7-8648000102C1865D

581 Ganzei, L. A., Razzhigaeva, N. G., Harlamov, A. A., & Ivel'skaya, T. N. (2010). Extreme storms in 2006–2007 on Shikotan
582 Island and their impact on the coastal relief and deposits. Oceanology, 50(3), 425–434.
583 https://doi.org/10.1134/S0001437010030112

584 Goldfinger, C., Ikeda, Y., Yeats, R. S., & Ren, J. (2013). Superquakes and Supercycles. Seismological Research Letters, 84(1),
585 24–32. https://doi.org/10.1785/0220110135

586 Goto, K., Hashimoto, K., Sugawara, D., Yanagisawa, H., & Abe, T. (2014). Spatial thickness variability of the 2011 Tohoku-oki
587 tsunami deposits along the coastline of Sendai Bay. Marine Geology, 358, 38–48. https://doi.org/10.1016/j.margeo.2013.12.015

588 Hashimoto, C., Noda, A., Sagiya, T., & Matsu'ura, M. (2009). Interplate seismogenic zones along the Kuril–Japan trench
589 inferred from GPS data inversion. Nature Geoscience, 2(2), 141–144. https://doi.org/10.1038/ngeo421

590 Hutchinson, I., & Clague, J. (2017). Were they all giants? Perspectives on late Holocene plate-boundary earthquakes at the
591 northern end of the Cascadia subduction zone. Quaternary Science Reviews, 169, 29–49.
592 https://doi.org/10.1016/j.quascirev.2017.05.015

593 Inman, H. F., & E. L. Bradly Jr. (1989). The overlapping coefficient as a measure of agreement between probability distributions
594 and point estimation of the overlap of two normal densities. Communications in Statistics - Theory and Methods, 18(10), 3851–
595 3874. https://doi.org/10.1080/03610928908830127

596 Ioki, K., & Tanioka, Y. (2016). Re-estimated fault model of the 17th century great earthquake off Hokkaido using tsunami
597 deposit data. Earth and Planetary Science Letters, 433, 133–138. https://doi.org/10.1016/j.epsl.2015.10.009

598 Ishizawa, T., Goto, K., Yokoyama, Y., Miyairi, Y., Sawada, C., Nishimura, Y., & Sugawara, D. (2017). Sequential radiocarbon
599 measurement of bulk peat for high-precision dating of tsunami deposits. Quaternary Geochronology, 41, 202–210.
600 https://doi.org/10.1016/j.quageo.2017.05.003

601 Ishizawa, T., Goto, K., Yokoyama, Y., & Goff, J. (2020). Dating tsunami deposits: Present knowledge and challenges. Earth-
602 Science Reviews, 200, 102971. https://doi.org/10.1016/j.earscirev.2019.10297

603 Jaffe, B. E., Goto, K., Sugawara, D., Richmond, B. M., Fujino, S., & Nishimura, Y. (2012). Flow speed estimated by inverse
604 modeling of sandy tsunami deposits: results from the 11 March 2011 tsunami on the coastal plain near the Sendai Airport,
605 Honshu, Japan. Sedimentary Geology, 282, 90–109. https://doi.org/10.1016/j.sedgeo.2012.09.002

606 Jagodziński, R., Sternal, B., Szczuciński, W., Lorenc, S. (2009). Heavy minerals in 2004 tsunami deposits on Kho Khao Island,
607 Thailand. Polish Journal of Environmental Studies, 18, 103–110.

608 Jagodziński, R., Sternal, B., Szczuciński, W., Chagué-Goff, C., & Sugawara, D. (2012). Heavy minerals in the 2011 Tohoku-oki
609 tsunami deposits—insights into sediment sources and hydrodynamics. Sedimentary Geology, 282, 57–64.
610 https://doi.org/10.1016/j.sedgeo.2012.07.015

611 Kelsey, H., Satake, K., Sawai, Y., Sherrod, B., Shimokawa, K., & Shishikura, M. (2006). Recurrence of postseismic coastal
612 uplift, Kuril subduction zone, Japan. Geophysical Research Letters, 33(13), L13315. https://doi.org/10.1029/2006GL026052

613 Koike, K. & Machida, H. (2001). Atlas of Quaternary Marine Terraces in the Japanese Islands: Tokyo, University of Tokyo Press
614 (in Japanese).

615 Lienkaemper, J. J., & Ramsey, C. B. (2009). OxCal: Versatile Tool for Developing Paleoearthquake Chronologies –A Primer.
616 Seismological Research Letters, 80(3), 431–434. https://doi.org/10.1785/gssrl.80.3.431

617 Liu, X., Zhao, D., & Li, S. (2013). Seismic heterogeneity and anisotropy of the southern Kuril arc: insight into megathrust
618 earthquakes. Geophysical Journal International, 194(2), 1069–1090. https://doi.org/10.1093/gji/ggt150

619 Morton, R. A., Gelfenbaum, G., & Jaffe, B. E. (2007). Physical criteria for distinguishing sandy tsunami and storm deposits using
620 modern examples. Sedimentary Geology, 200(3–4), 184–207. https://doi.org/10.1016/j.sedgeo.2007.01.003

621 Nakamura, Y., Nishimura, Y., & Putra, P. S. (2012). Local variation of inundation, sedimentary characteristics, and mineral
622 assemblages of the 2011 Tohoku-oki tsunami on the Misawa coast, Aomori, Japan. Sedimentary Geology, 282, 216–227.
623 https://doi.org/10.1016/j.sedgeo.2012.06.003

624 Nakanishi, R., Okamura, S., Yokoyama, Y., Miyairi, Y., Sagayama, T., & Ashi, J. (2020a). Holocene tsunami, storm, and relative
625 sea level records obtained from the southern Hidaka coast, Hokkaido, Japan. Quaternary Science Reviews, 250, 106678.
626 https://doi.org/10.1016/j.quascirev.2020.106678

627 Nakanishi, R., Ashi, J., & Okamura, S. (2020b). A dataset for distribution and characteristics of Holocene pyroclastic fall
628 deposits along the Pacific coasts in western Hokkaido, Japan. Data in Brief, 33, 106565.
629 https://doi.org/10.1016/j.dib.2020.106565

630 Nanayama, F., Satake, K., Furukawa, R., Shimokawa, K., Atwater, B. F., Shigeno, K., & Yamaki, S. (2003). Unusually large
631 earthquakes inferred from tsunami deposits along the Kuril trench. Nature, 424(6949), 660–663.
632 https://doi.org/10.1038/nature01864

633 Nanayama, F., Furukawa, R., Shigeno, K., Makino, A., Soeda, Y., & Igarashi, Y. (2007). Nine unusually large tsunami deposits
634 from the past 4000 years at Kiritappu marsh along the southern Kuril Trench. Sedimentary Geology, 200(3–4), 275–294.
635 https://doi.org/10.1016/j.sedgeo.2007.01.008

636 Naruse, H., & Abe, T. (2017). Inverse Tsunami Flow Modeling Including Nonequilibrium Sediment Transport, With Application
637 to Deposits From the 2011 Tohoku-Oki Tsunami. Journal of Geophysical Research: Earth Surface, 122(11), 2159–2182.
638 https://doi.org/10.1002/2017JF004226

639 Nelson, A. R., Kelsey, H. M., & Witter, R. C. (2006). Great earthquakes of variable magnitude at the Cascadia subduction zone.
640 Quaternary Research, 65(3), 354–365. https://doi.org/10.1016/j.yqres.2006.02.009

641 Nishimura, Y., & Miyaji, N. (1996). Investigations of storm deposits caused by a typhoon of September 19th, 1994. Bulletin of
642 the Natural Disaster Science Data Center, Hokkaido, 10, 15–26 (in Japanese, with English abstract).

643 Nishimura Y., Tanioka Y., & Hirakawa K. (2004). Beachside Trace for the 2003 Tokachi-oki Tsunami Run-up. Zisin (Journal of
644 the Seismological Society of Japan. 2nd ser.), 57(2), 135–138. https://doi.org/10.4294/zisin1948.57.2_135

645 Okada, Y. (1985). Surface deformation due to shear and tensile faults in a half-space, Bulletin of the Seismological Society of
646 America, 75, 1135–1154.

Okuno, J., Nakada, M., Ishii, M., & Miura, H. (2014). Vertical tectonic crustal movements along the Japanese coastlines inferred from late Quaternary and recent relative sea-level changes. Quaternary Science Reviews, 91, 42–61. https://doi.org/10.1016/j.quascirev.2014.03.010

Philibosian, B., & Meltzner, A. J. (2020). Segmentation and supercycles: A catalog of earthquake rupture patterns from the Sumatran Sunda Megathrust and other well-studied faults worldwide. Quaternary Science Reviews, 241, 106390. https://doi.org/10.1016/j.quascirev.2020.106390

Reimer, P. J., Austin, W. E. N., Bard, E., Bayliss, A., Blackwell, P. G., Ramsey, C. B., et al. (2020). The IntCal20 Northern Hemisphere Radiocarbon Age Calibration Curve (0–55 cal kBP). Radiocarbon, 62(4), 725–757. https://doi.org/10.1017/RDC.2020.41

Richmond, B., Szczuciński, W., Chagué-Goff, C., Goto, K., Sugawara, D., Witter, R., et al. (2012). Erosion, deposition and landscape change on the Sendai coastal plain, Japan, resulting from the March 11, 2011 Tohoku-oki tsunami. Sedimentary Geology, 282, 27–39. https://doi.org/10.1016/j.sedgeo.2012.08.005

Sakuraba, H. (2019). Cape Erimo National Forest Management Project (Erimo Town, Hokkaido), Suirikagaku, 62, 119–124 (in Japanese). https://doi.org/10.20820/suirikagaku.62.6_119

Salditch, L., Stein, S., Neely, J., Spencer, B. D., Brooks, E. M., Agnon, A., & Liu, M. (2020). Earthquake supercycles and Long-Term Fault Memory. Tectonophysics, 774, 228–289. https://doi.org/10.1016/j.tecto.2019.228289

Satake, K. (2015). Geological and historical evidence of irregular recurrent earthquakes in Japan. Philosophical Transactions of the Royal Society A: Mathematical, Physical and Engineering Sciences, 373(2053), 20140375. https://doi.org/10.1098/rsta.2014.0375

Satake, K., Nanayama, F., & Yamaki, S. (2008). Fault models of unusual tsunami in the 17th century along the Kuril trench. Earth, Planets and Space, 60(9), 925–935. https://doi.org/10.1186/BF03352848

Satake, K., Fujii, Y., Harada, T., Namegaya, N. (2013). Time and Space Distribution of Coseismic Slip of the 2011 Tohoku Earthquake as Inferred from Tsunami Waveform Data. Bulletin of the Seismological Society of America, 103 (2B), 1473–1492. https://doi.org/10.1785/0120120122

Sawai, Y., Satake, K., Kamataki, T., Nasu, H., Shishikura, M., Atwater, B. F., et al. (2004). Transient Uplift After a 17th-Century Earthquake Along the Kuril Subduction Zone. Science, 306(5703), 1918–1920. https://doi.org/10.1126/science.1104895

Sawai, Y., Kamataki, T., Shishikura, M., Nasu, H., Okamura, Y., Satake, K., et al. (2009). Aperiodic recurrence of geologically recorded tsunamis during the past 5500 years in eastern Hokkaido, Japan. Journal of Geophysical Research: Solid Earth, 114, B01319. https://doi.org/10.1029/2007JB005503

Sawai, Y. (2020). Subduction zone paleoseismology along the Pacific coast of northeast Japan — progress and remaining problems. Earth-Science Reviews, 208, 103261. https://doi.org/10.1016/j.earscirev.2020.103261

Sella, G. F., Dixon, T. H., & Mao, A. (2002). REVEL: A model for Recent plate velocities from space geodesy: REVEL-RECENT PLATE VELOCITIES FROM SPACE GEODESY. Journal of Geophysical Research: Solid Earth, 107(B4), ETG 11-1-ETG 11-30. https://doi.org/10.1029/2000JB000033

Shigeno, K., & Nanayama, F. (2016). Sedimentary Process of a Small Sandy Event Deposit due to a Storm Surge and Storm Waves Generated by a Typhoon: An Example from the Hirahama Coastal Lowland along the Western Example from the Hirahama Coastal Lowland along the Western Coast of the Oshima Peninsula between 09:00 September 18 and 01:00 September 19, 1959. Journal of Geography (Chigaku Zasshi), 125, 747–762 (in Japanese, with English abstract). https://doi:10.5026/jgeography.125.747

Sieh, K., Natawidjaja, D. H., Meltzner, A. J., Shen, C.-C., Cheng, H., Li, K.-S., et al. (2008). Earthquake Supercycles Inferred from Sea-Level Changes Recorded in the Corals of West Sumatra. Science, 322(5908), 1674–1678. https://doi.org/10.1126/science.1163589

689 Soria, J. L. A., Switzer, A. D., Pilarczyk, J. E., Siringan, F. P., Khan, N. S., & Fritz, H. M. (2017). Typhoon Haiyan overwash
690 sediments from Leyte Gulf coastlines show local spatial variations with hybrid storm and tsunami signatures. Sedimentary
691 Geology, 358, 121–138. https://doi.org/10.1016/j.sedgeo.2017.06.006

692 Soria, J. L. A., Switzer, A. D., Pilarczyk, J. E., Tang, H., Weiss, R., Siringan, F., et al. (2018). Surf beat-induced overwash during
693 Typhoon Haiyan deposited two distinct sediment assemblages on the carbonate coast of Hernani, Samar, central Philippines.
694 Marine Geology, 396, 215–230.

695 Szczuciński, W. (2020). Post-depositional changes to tsunami deposits and their preservation potential. In M. Engel, J. Pilarczyk,
696 S. Matthias, M. D. Brill, & Ed Garrett (Eds.), Geological records of tsunamis and other extreme waves. Elsevier.
697 https://doi.org/10.1016/B978-0-12-815686-5.00021-3

698 Szczuciński, W., Kokociński, M., Rzeszewski, M., Chagué-Goff, C., Cachão, M., Goto, K., & Sugawara, D. (2012). Sediment
699 sources and sedimentation processes of 2011 Tohoku-oki tsunami deposits on the Sendai Plain, Japan — Insights from diatoms,
700 nannoliths and grain size distribution. Sedimentary Geology, 282, 40–56. https://doi.org/10.1016/j.sedgeo.2012.07.019

701 Szczuciński, W., Pawłowska, J., Lejzerowicz, F., Nishimura, Y., Kokociński, M., Majewski, W., Nakamura, Y., Pawlowski, J.,
702 2016. Ancient sedimentary DNA reveals past tsunami deposits. Marine Geology, 381, 29–33. https://doi.org/10.1016/j.
703 margeo.2016.08.00

704 Switzer, A. D., Felix, R. P., Soria, J. L. A., & Shaw, T. A. (2020). A comparative study of the 2013 typhoon Haiyan overwash
705 sediments from a coastal cave and beach system at Salcedo, Eastern Samar, central Philippines. Marine Geology, 419, 106083.
706 https://doi.org/10.1016/j.margeo.2019.106083

707 Takada, K., Nakata, T., Miyagi, T., Haraguchi, T. & Nishitani, Y. (2002). Handy Geoslicer—new soil sampler for Quaternary
708 geologist. Chishitsu News, 579, 12-18 (in Japanese).

709 Takashimizu, Y., Urabe, A., Suzuki, K., & Sato, Y. (2012). Deposition by the 2011 Tohoku-oki tsunami on coastal lowland
710 controlled by beach ridges near Sendai, Japan. Sedimentary Geology, 282, 124–141.
711 https://doi.org/10.1016/j.sedgeo.2012.07.004

712 Tanioka, Y., Nishimura, Y., Hirakawa, K., Imamura, F., Abe, I., Abe, Y., et al. (2004). Tsunami run-up heights of the 2003
713 Tokachi-oki earthquake. Earth, Planets and Space, 56(3), 359–365. https://doi.org/10.1186/BF03353065

714 Watanabe, M., Goto, K., Bricker, J. D., & Imamura, F. (2018). Are inundation limit and maximum extent of sand useful for
715 differentiating tsunamis and storms? An example from sediment transport simulations on the Sendai Plain, Japan. Sedimentary
716 Geology, 364, 204–216. https://doi.org/10.1016/j.sedgeo.2017.12.026

717 Wessel, P., Smith, W. H. F., Scharroo, R., Luis, J., & Wobbe, F. (2013). Generic Mapping Tools: Improved version released.
718 Eos, Transactions American Geophysical Union, 94(45), 409–410. https://doi.org/10.1002/2013EO450001

719 Yoshii, T., Tanaka, S., & Matsuyama, M. (2017). Tsunami deposits in a super-large wave flume. Marine Geology, 391, 98–107.
720 https://doi.org/10.1016/j.margeo.2017.07.020

721 Yokoyama, Y., Miyairi, Y., Aze, T., Yamane, M., Sawada, C., Ando, Y., et al. (2019). A single stage Accelerator Mass
722 Spectrometry at the Atmosphere and Ocean Research Institute, The University of Tokyo. Nuclear Instruments and Methods in
723 Physics Research Section B: Beam Interactions with Materials and Atoms, 455, 311–316.
724 https://doi.org/10.1016/j.nimb.2019.01.055

725